



Multi-strategy for constructing Z-scheme porous hollow double-shell Fe₂O₃@Ov-NiFe₂O₄ nanorods-arrays photocathode: Bias-free synthesis of H₂O₂, Zn-H₂O₂ cell and generation of NaZnPO₄

Xue Feng, Lei Zhang *

College of Chemistry, Liaoning University, 66 Chongshan Middle Road, Shenyang 110036, China



ARTICLE INFO

Keywords:
Porous double-shell hollow nanorods arrays
Oxygen vacancies
Strongly coupled interface structure
Z-scheme charge transfer
H₂O₂ and NaZnPO₄ generation

ABSTRACT

The rational design of highly active and cost-effective catalysts for the photoelectrocatalytic H₂O₂ production plays a crucial role in the development of sustainable energy. An in situ self-assembly template and coupling strategy are demonstrated to design a novel porous hollow double-shell Fe₂O₃ @Ov-NiFe₂O₄ with enriched oxygen vacancies and a strongly coupled interface (PDS-Fe₂O₃ @Ov-NiFe₂O₄-HR) for producing chemical value-added product and constructing rechargeable Zn-H₂O₂ batteries. As-resultant Z-scheme PDS-Fe₂O₃ @Ov-NiFe₂O₄-HR, by improving light utilization efficiency, redox ability and interfacial charge separation efficiency has fast interfacial carrier transport and low electrochemical resistance, thus kinetically promoting PEC can sustain high H₂O₂ production rates (6.3 mM h⁻¹). Furthermore, the combined configuration of PDS-Fe₂O₃ @Ov-NiFe₂O₄-HR-Ti and Fe₂O₃-Ti enable the production of H₂O₂ on both electrodes under an external bias-free condition. Zn-H₂O₂ cells can also provide sufficient power to a light-emitting diode. This rational design strategy provides a new path for constructing highly efficient heterostructure catalysts on energy-related devices.

1. Introduction

Hydrogen peroxide (H₂O₂) as an eco-friendly oxidant and potential energy carrier has been widely applied in many environmental, energy and chemical applications [1–3]. With the increasing demand for H₂O₂ in industrial production, it is imperative to develop environmentally friendly and benign synthesis methods [4–6]. Currently, photoelectrochemical (PEC) methods have been reported to be the most promising and the highest efficiency approaches for producing green H₂O₂ via the oxygen reduction reaction (ORR) and the water oxidation reaction (WOR) with photogenerated electrons, holes in the photocathode and photoanode, respectively [7–9].

Usually, various nanostructured semiconductors and their composites, including Cu₃BiS₃ photocathode [10], CuBi₂O₄ photocathode [11], core-shell MoSe₂/TiO₂ nanorod arrays photocathode [12], BiVO₄ photoanode [13–15], FeO(OH)/BiVO₄ photoanode [16] and WO₃/BiVO₄ photoanode [17] were successfully used for PEC H₂O₂ production. In this context, among the investigated morphology, the hollow shell nanostructured semiconductors are an attractive morphology to enhance the PEC performance, just that large interior cavity can cause the multi-light reflection to enhance photoabsorption, the cavity in the

hollow structures can afford high specific surface areas for redox reactions, maximization of interface area can improve the separation efficiency of charge at the interface between solids and provide large contact interfaces between the electrocatalyst and the electrolyte [18–20]. Lee et al. synthesized Ir-Co₃O₄ @Co₃O₄ porous core-shell hollow sphere, and this electrocatalyst revealed excellent catalytic activity toward OER in acid media [21]. Furthermore, Feng et al. studied that the synthesized cactuslike NiCo₂S₄ @NiFe LDH hollow sphere presented significant bifunctional electrocatalytic performances for both ORR and OER [22]. Ma et al. reported that carbon dots loaded acidic titania hollow nanotubes presented significant photocatalytic H₂O₂ synthesis [23]. Zhang et al. reported that the nitrogen-doped hollow carbon polyhedron hybrid exhibits excellent 2e⁻ ORR electrocatalytic activity with high selectivity of up to 92.6 % [24].

However, most core-shell nanostructured heterojunction catalysts have fewer contact sites, so it is difficult to form a strong coupling interface for enhancing the efficiency of charge separation and improving the PEC activity. Therefore, the formation of strong coupling interfaces in the designed nanomaterials also plays a significant role in the regulation of the PEC properties [25–27]. Wang et al. reported that interfacial chemical bond (Mo-S) of Sv-ZnIn₂S₄/MoSe₂ could be applied

* Corresponding author.

E-mail address: zhanglei63@126.com (L. Zhang).

for enhancing photocatalytic hydrogen evolution [28]. Li et al. reported that the $\text{Bi}_2\text{WO}_6/\text{InVO}_4$ with 2D/2D coupling interface exhibited excellent photocatalytic CO_2 reduction and stability [29]. Huang et al. reported that the thin-walled hollow nanotube structure $\text{Fe}_2\text{O}_3/\text{MoO}_3$ with a CH_3OH to HCHO selectivity of 95.7 %, the Fe-O-Mo charge transfer channel and internal electric field in the $\text{Fe}_2\text{O}_3/\text{MoO}_3$ interface improve charge transfer efficiency [30].

Furthermore, the introduction of convertible valence elements could change the reaction process and reduce the activation energy, thus greatly improving the surface reaction effect. Ion pairs $\text{Co}^{2+}/\text{Co}^{3+}$, $\text{Ni}^{2+}/\text{Ni}^{3+}$ and $\text{Fe}^{2+}/\text{Fe}^{3+}$ are often used to facilitate the reaction [31–33]. Zhang et al. reported that the $\text{Ni}^{2+}/\text{Ni}^{3+}$ redox of $\text{Cu}_x\text{O}@\text{NiFe-LDH}$ for oxygen evolution (OER) and (ORR), improving Zn-Air batteries efficiency and lifetime [34]. Du et al. reported the $\text{Ni}^{2+}/\text{Ni}^{3+}$ redox of inhomogeneous NiFe-LDH for energetic oxygen Evolution, improving efficiency and stability of Zn-Air batteries [35].

Here, we designed a strongly coupled interface, porous double-shell hollow photoelectrocatalyst with elements of transformable valence using the multistep MOF-engaged strategy for multifunctional applications, including H_2O_2 production and rechargeable Zn- H_2O_2 battery with supercatalytic performance and the generation of high-value chemicals NaZnPO_4 . The hollow double-shell O-vacancies $\text{Fe}_2\text{O}_3 @\text{NiFe}_2\text{O}_4\text{-Ti}$ nanorods arrays (PDS- $\text{Fe}_2\text{O}_3 @\text{Ov-NiFe}_2\text{O}_4\text{-HR-Ti}$) as photocathode can improve photocurrent property to enhance the H_2O_2 generation. Moreover, we also recently focused on developing a versatile and stand-alone PEC system for producing H_2O_2 on both the photocathode and photoanode, using only H_2O and O_2 as raw materials, under simulated solar light without applied voltage. Simultaneously, the PDS- $\text{Fe}_2\text{O}_3 @\text{Ov-NiFe}_2\text{O}_4\text{-HR-Ti}$ photocathode presents a high power density of 12 mW cm^{-2} and co-produces high-value chemicals of NaZnPO_4 for rechargeable Zn- H_2O_2 batteries with alkaline and neutral as electrolyte.

2. Experimental section

2.1. Fabrication of photoelectrodes

2.1.1. Synthesis of MIL-88-Ti photoelectrode

For the preparation of the MIL-88-Ti electrode, a piece of precleaned Ti net ($2 \times 2 \text{ cm}^2$) was immersed in mixed solution of 0.07 M fumaric acid and 0.1 M $\text{Fe}(\text{NO}_3)_3 \cdot 9 \text{ H}_2\text{O}$, then transferred into a Teflon-lined autoclave (40 mL in capacity) and heated to 110 °C for 6 h. After cooling down to room temperature, the MIL-88-Ti was obtained.

2.1.2. Synthesis of MIL-88 @FeFe PB-Ti photoelectrode

In a typical synthesis, 1.0 g of polyvinylpyrrolidone (PVP, K30), 120 mg of $\text{K}_3[\text{Fe}(\text{CN})_6]$ and 0.4 mL concentrated hydrochloric acid were dissolved in ethanol/distilled water (30.0 mL, 1/2 v/v) under magnetic stirring. Then MIL-88-Ti was added to the above solution. After stirring for 10 min, the resulting solution was transferred to a Teflon-lined autoclave and kept at 80 °C for 12 h. The MIL-88 @FeFe PB-Ti electrode was washed with ethanol several times and dried at 70 °C for further use.

2.1.3. Synthesis of MIL-88 @FeFe@NiFe PBA-Ti photoelectrode

For the preparation of the MIL-88 @FeFe@NiFe PBA-Ti electrode, 142 mg of $\text{NiCl}_2 \cdot 6 \text{ H}_2\text{O}$, 0.25 g of sodium citrate and 0.3 g of PVP (K30) were added to form solution A. Then, MIL-88 @FeFe PBA-Ti electrode was added to the above solution A. Meanwhile, 66 mg of $\text{K}_3[\text{Fe}(\text{CN})_6]$ was dissolved in 20 mL of distilled water to form solution B. Subsequently, solution B was slowly added to solution A, under magnetic stirring. The resulting solution was aged for 24 h at room temperature without any interruption. The MIL-88 @FeFe@NiFe PBA-Ti electrode was collected, washed with distilled water and ethanol several time for further use.

2.1.4. Synthesis of PDS- $\text{Fe}_2\text{O}_3 @\text{Ov-NiFe}_2\text{O}_4\text{-HR-Ti}$ photoelectrode

For the preparation of the PDS- $\text{Fe}_2\text{O}_3 @\text{Ov-NiFe}_2\text{O}_4\text{-HR-Ti}$ photoelectrode, MIL-88 @FeFe@NiFe PBA-Ti photoelectrode was added to 15 mL of 0.1 M NaOH solution and then shaken by hand for several minutes. After the color turned yellow, the MIL-88 @ $\text{Fe}(\text{OH})_3 @\text{NiFe}$ PBA-Ti electrode was washed with distilled water and ethanol several times. Then the MIL-88 @ $\text{Fe}(\text{OH})_3 @\text{NiFe}$ PBA-Ti was added into 15 mL of concentrated hydrochloric acid, the MIL-88 @NiFe PBA-Ti photoelectrode after reaction 20 min was obtained, which was heated at 450 °C for 2 h under ambient air. Similarly, a contrast sample (PDS- $\text{Fe}_2\text{O}_3 @\text{Ov-NiFe}_2\text{O}_4\text{-HR}$) was prepared without Ti net. The NiFe_2O_4 and $\text{Fe}_2\text{O}_3/\text{NiFe}_2\text{O}_4$ without oxygen vacancies were prepared by hydrothermal method [36].

2.1.5. Synthesis of photoanodes

For the preparation of the $\text{Fe}_2\text{O}_3\text{-Ti}$ photoanode, the MIL-88-Ti electrode was heated at 450 °C for 2 h under ambient air to obtain the $\text{Fe}_2\text{O}_3\text{-Ti}$ photoelectrode. Other photoanodes were synthesized according to the literature that has been reported [37,38].

2.2. PEC H_2O_2 production by the PDS- $\text{Fe}_2\text{O}_3 @\text{Ov-NiFe}_2\text{O}_4\text{-HR-Ti}$ photocathode

The PEC performance of the PDS- $\text{Fe}_2\text{O}_3 @\text{Ov-NiFe}_2\text{O}_4\text{-HR-Ti}$ electrode was investigated in a three-electrode configuration by using a silver-silver chloride (Ag/AgCl) reference electrode and a Pt counter electrode. Electrolytes were 0.1 M Na_2SO_4 solution (20 mL, pH = 3–9 with 1 M HClO_4 or KOH) or 1 M PBS solution. All electrolytes were stirred and purged with O_2 gas for 30 min prior to PEC measurement. The photocathode was illuminated under 300 W Xe arc lamp adjusted to 100 mW cm^{-2} . The amount of produced H_2O_2 was recorded using spectroscopic titration as the following stated. Fig. S1 shows the standard fitted curve of different H_2O_2 concentrations.

2.3. PEC H_2O_2 production by photocathode-anode coupling

PEC H_2O_2 production was performed in both photoanode and photocathode, which was separated by a Nafion membrane. The $\text{Fe}_2\text{O}_3\text{-Ti}$ photoanode and the as-prepared PDS- $\text{Fe}_2\text{O}_3 @\text{Ov-NiFe}_2\text{O}_4\text{-HR-Ti}$ photocathode for selective electrocatalytic water oxidation and O_2 reduction to produce H_2O_2 in N_2 -saturated KHCO_3 solution (20 mL) and O_2 -saturated Na_2SO_4 solution (20 mL) were studied. The total amount of produced H_2O_2 was recorded using spectroscopic titration.

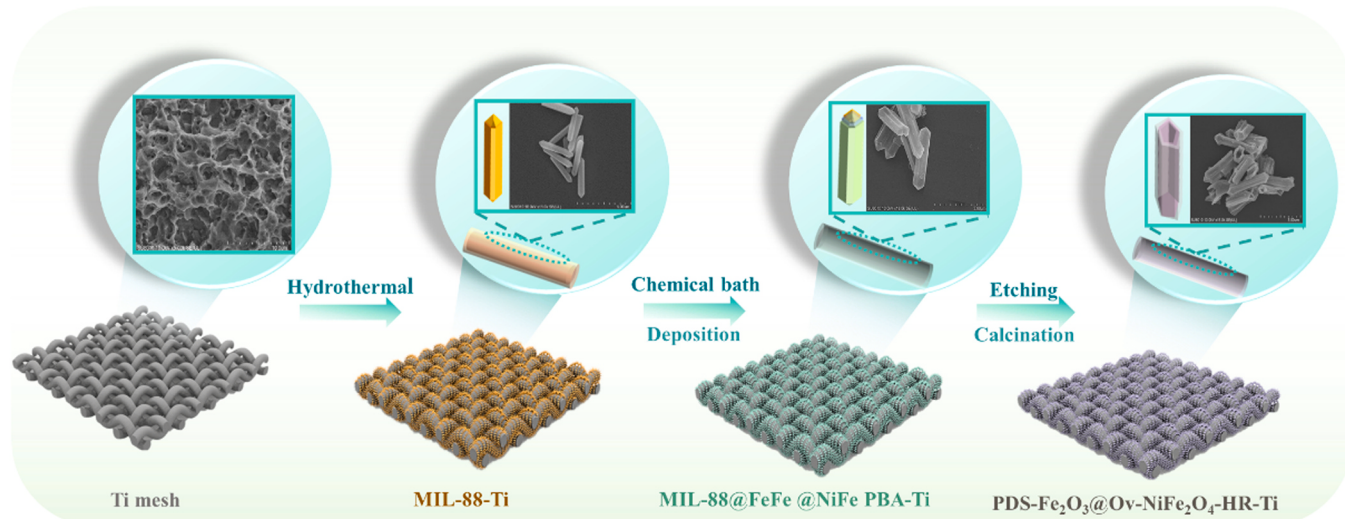
2.4. Zn- H_2O_2 battery measurements

The measurements of Zn- H_2O_2 batteries were tested in homemade electrochemical cells under ambient conditions. The as-prepared PDS- $\text{Fe}_2\text{O}_3 @\text{Ov-NiFe}_2\text{O}_4\text{-HR-Ti}$ ($2 \times 2 \text{ cm}^2$) and Zn plate ($2 \times 2 \text{ cm}^2$) were used as the work photocathode and the anode. The electrolyte are 6.0 M KOH solution containing 0.2 M zinc acetate or 1 M PBS solution (pH=6) consisting of NaH_2PO_4 and Na_2HPO_4 .

3. Results and discussion

3.1. Materials characterization

The synthesis route of the porous hollow double-shell $\text{Fe}_2\text{O}_3 @\text{NiFe}_2\text{O}_4$ nanorods arrays on Ti mesh is illustrated in Scheme 1. First, MIL-88 nanorods arrays were grown on Ti mesh as template and seed crystal using a hydrothermal route. Second, FeFe PB and NiFe PBA were layer-by-layer wrapped around MIL-88 nanorods arrays through epitaxial deposition to construct core double-shell MIL-88 @FeFe PB@NiFe PBA nanorods arrays. Then, the core double-shell MIL-88 @ $\text{Fe}(\text{OH})_3 @\text{NiFe}$ PBA nanorods are obtained by the reaction between FeFe PB and NaOH solution, leading to the formation of a thin layer of Fe



Scheme 1. Illustration of synthesis strategy for PDS-Fe₂O₃ @Ov-NiFe₂O₄-HR-Ti.

(OH)₃ on the surface of MIL-88 nanorods. Finally, the porous hollow double-shell Fe₂O₃ @NiFe₂O₄ with enriched oxygen vacancies nanorods arrays on Ti mesh (PDS-Fe₂O₃ @Ov-NiFe₂O₄-HR-Ti) was prepared by washing with HCl solution and pyrolysis (450 °C).

The SEM images confirm that the MIL-88 nanorods were high-density and uniformly grown on the backbone of the Ti mesh with a diameter of approximately 500 nm (Fig. 1A-B). With FeFe PB and NiFe PBA orderly wrapped on the surface of MIL-88 nanorods, the diameter of

the MIL-88 nanorods was increased to 1 μm (Fig. 1C-F). Finally, with the anion exchange reaction, acid etching and calcination, the morphology of hollow double shell Fe₂O₃ @Ov-NiFe₂O₄ was observed on the Ti mesh (Fig. 1G-H). As shown in Fig. S2, the Brunauer-Emmett-Teller (BET) surface areas of the core-shell MIL-88 @NiFe PBA and PDS-Fe₂O₃ @Ov-NiFe₂O₄-HR are 38.89 and 84.32 m² g⁻¹, respectively. The improvement of large specific surface area could be attributed to the formation of hollow porous double-shell structure via a self-templating

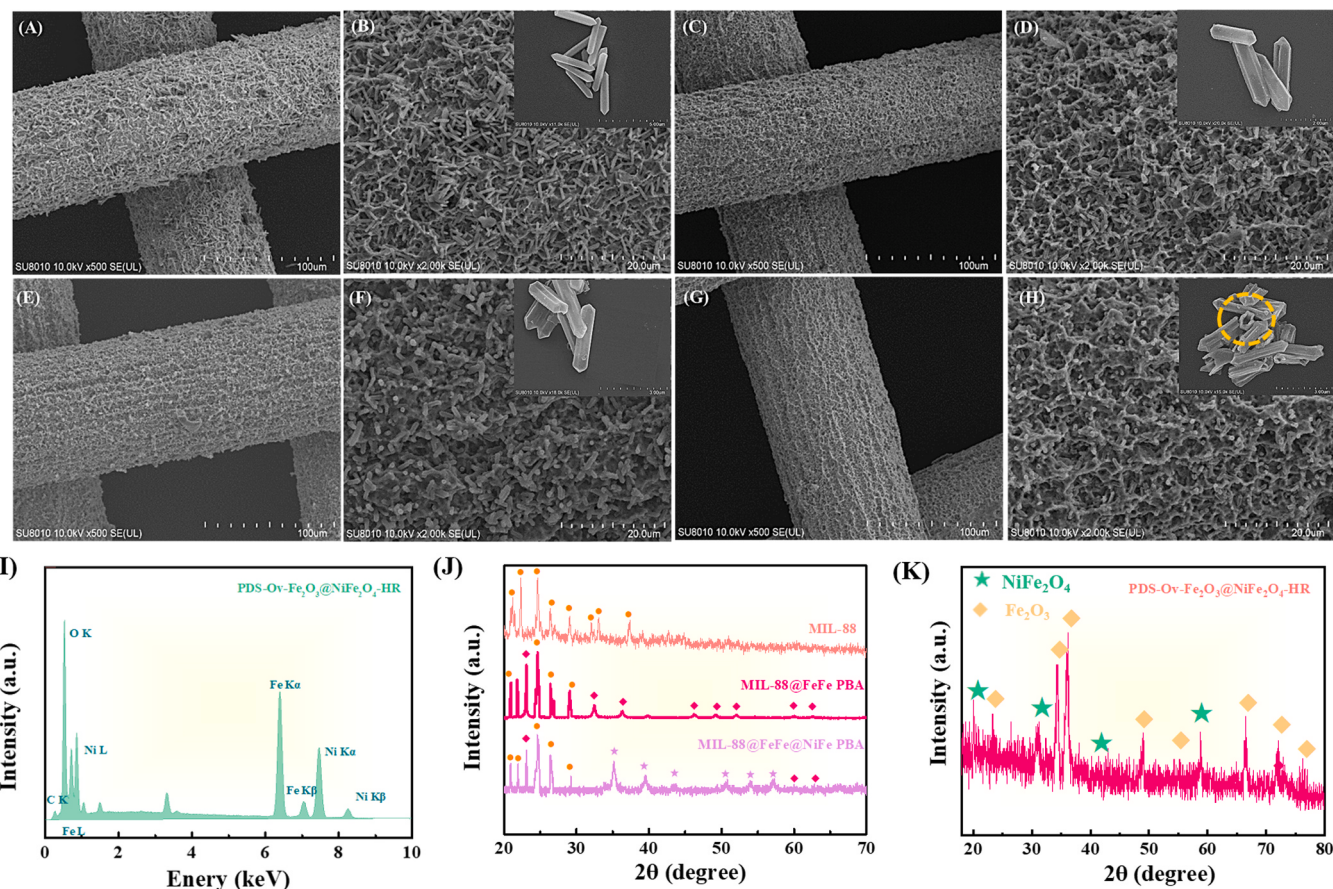


Fig. 1. SEM images of MIL-88-Ti (A-B), MIL-88 @FeFe PB-Ti (C-D), MIL-88 @FeFe@NiFe PBA-Ti (E-F), and PDS-Fe₂O₃ @Ov-NiFe₂O₄-HR-Ti (G-H), EDS of PDS-Fe₂O₃ @Ov-NiFe₂O₄-HR (I), XRD pattern of electrodes (J), XRD pattern of the PDS-Fe₂O₃ @Ov-NiFe₂O₄-HR (K).

pyrolysis in air atmosphere [39]. The pore size distributions of both samples indicate their mesoporous structure (Fig. S2 inset). The unique hollow double shell structure could improve light-absorption capability, reduce charge-transfer distance and direct separation of charge carriers for charge recombination suppression; high surface areas and multilevel shell surfaces for spatial redox reactions for accelerating surface reactions. Moreover, the morphology of Ti net revealed that it maintained its structural strength during the hydrothermal synthesis, anion exchange reaction, acid etching and calcination, thus demonstrating its robustness and validating its anchoring role (Fig. 1A, C, E, G). EDS analysis illustrates the existence and uniform distribution of Fe, Ni and O elements in PDS-Fe₂O₃ @Ov-NiFe₂O₄-HR (Fig. 1I). Specifically, MIL-88 nanorod arrays were grown on Ti substrate, and confirmed by X-ray diffraction (XRD) pattern (Fig. 1J) [40]. In addition, it is evident that all diffraction peaks of MIL-88 @FeFe PB and MIL-88 @FeFe@NiFe PBA could be indexed to FeFe PB (JCPDS: 73-0687) and NiFe PBA (JCPDS: 86-0501) [41,42]. After etching, acid pickling and pyrolysis, introducing Fe₂O₃ (JCPDS: 1-089-0597) [43] and Ov-NiFe₂O₄ phase (JCPDS: 04-0784) [44] indicated that the successful synthesis of PDS-Fe₂O₃ @Ov-NiFe₂O₄-HR photocathode.

The surface chemical states and composition of the Fe₂O₃, Ov-NiFe₂O₄ and PDS-Fe₂O₃ @Ov-NiFe₂O₄-HR were studied with X-ray photoelectron spectroscopy (XPS). As can be found from the survey spectrum (Fig. S3), the Fe, Ni and O peaks are observed in PDS-Fe₂O₃ @Ov-NiFe₂O₄-HR, which is agreement with the EDS results. The peaks of the Fe 2p spectrum located at 711.5 and 725.5 eV, 712.5 and 726.5 eV for Fe₂O₃ and Ov-NiFe₂O₄ in Fig. 2A match well with the Fe 2p_{3/2} and Fe 2p_{1/2} of Fe²⁺/Fe³⁺, respectively [43,44]. With the formation of PDS-Fe₂O₃ @Ov-NiFe₂O₄-HR, the bending energy of Fe 2p_{1/2} and Fe 2p_{3/2} display a positive shift of about 0.6 eV compared to Fe₂O₃ (Fig. 2B), which is related to the loss of electrons from Fe of Fe₂O₃ atoms. Simultaneously, the peaks of Ni 2p spectrum located at 855.2 and 874.9 eV for Ov-NiFe₂O₄ in Fig. 2B match well with the Ni 2p_{3/2} and Ni

2p_{1/2} of Ni²⁺/Ni³⁺, respectively [44]. With the formation of PDS-Fe₂O₃ @Ov-NiFe₂O₄-HR, the bending energy of Ni 2p_{3/2} displays negative shift compared to Ov-NiFe₂O₄ (Fig. 2B), indicating the electrons tend to transfer from Fe₂O₃ to Ov-NiFe₂O₄. The clear electron transfer route suggested the formation of PDS-Fe₂O₃ @Ov-NiFe₂O₄-HR with a strong interface interaction [30]. The O 1 s spectrum in Fig. 2C can be deconvoluted into two peaks of Fe₂O₃ at about 529.1 and 531.5 eV, which belong to the Metal-O (M-O) and adsorbed O, respectively [43]. Furtherly, it can be noted that the peaks of M-O of PDS-Fe₂O₃ @Ov-NiFe₂O₄-HR exhibited a negative shift compared to Fe₂O₃ and Ov-NiFe₂O₄, implying that the PDS-Fe₂O₃ @Ov-NiFe₂O₄-HR heterojunction interactions were achieved via the O atom bridging the Fe of Fe₂O₃ and the Ni of NiFe₂O₄ to form strongly coupled interface (Fe-O-Ni). The Raman spectrum (Fig. S4) of Fe₂O₃, Ov-NiFe₂O₄ and PDS-Fe₂O₃ @Ov-NiFe₂O₄-HR also confirm the successful synthesis of PDS-Fe₂O₃ @Ov-NiFe₂O₄-HR heterojunction with interfacial Fe-O-Ni interface [45,46]. Subsequently, O vacancies (531.1 eV) are observed in the PDS-Fe₂O₃ @Ov-NiFe₂O₄-HR (Fig. 2C). The O vacancies can serve as strong electron-withdrawing group for facilitating the electrons transfer to O-vacancies. To further shed light on the O vacancies, the Fe₂O₃, Ov-NiFe₂O₄ and PDS-Fe₂O₃ @Ov-NiFe₂O₄-HR were investigated by electron spin-resonance (ESR) spectroscopy. As displayed in Fig. 2D, Ov-NiFe₂O₄ and PDS-Fe₂O₃ @Ov-NiFe₂O₄-HR both appeared obvious signal at g = 2.003, implied the existence of O vacancies [47]. The O vacancies in Ov-NiFe₂O₄ were verified as electron traps to capture the photogenerated electrons, thus prolonging the charge carriers lifetime. With the formation of O vacancies and Fe-O-Ni interface, the concentration of charge carriers is increased, which promotes the energy band bending and improves the separation efficiency of charge carriers. Moreover, the PDS-Fe₂O₃ @Ov-NiFe₂O₄-HR electrode could provide Ni²⁺/Ni³⁺ and Fe²⁺/Fe³⁺ redox pairs, concurrently facilitating to expose more active sites by the multichannel contacts, which improving electrocatalytic activity.

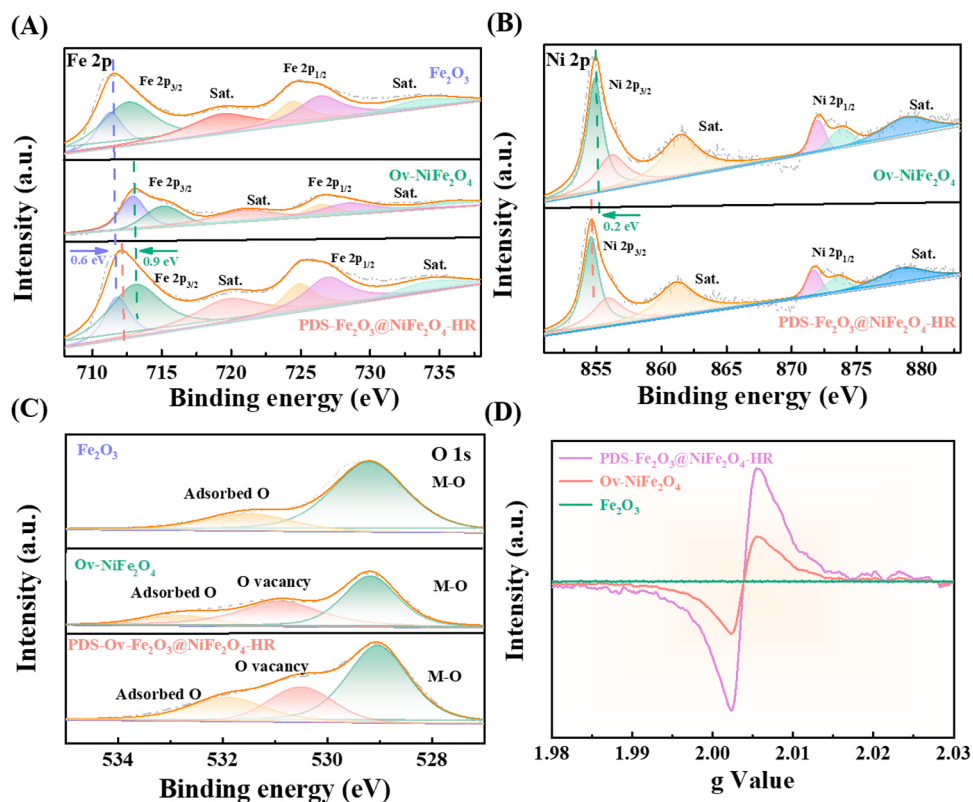


Fig. 2. XPS survey spectra of the Fe₂O₃, Ov-NiFe₂O₄ and PDS-Fe₂O₃ @Ov-NiFe₂O₄-HR of Fe 2p (A), Ni 2p (B) and O 1 s (C), ESR spectra of Fe₂O₃, Ov-NiFe₂O₄ and PDS-Fe₂O₃ @Ov-NiFe₂O₄-HR (D).

In order to study the photocatalytic activity of the catalysts, Fe_2O_3 , $\text{Ov-NiFe}_2\text{O}_4$ and $\text{PDS-Fe}_2\text{O}_3 @\text{Ov-NiFe}_2\text{O}_4-\text{HR}$ are inspected by UV-vis DRS. The $\text{PDS-Fe}_2\text{O}_3 @\text{Ov-NiFe}_2\text{O}_4-\text{HR}$ reveals better absorption performance in the UV-visible region with unique hollow double shell structure to achieve a higher utilization capacity for the UV-visible light (Fig. 3 A). The values of the band gap energy (E_g) were estimated to be 2.0 eV and 1.5 eV for Fe_2O_3 and $\text{Ov-NiFe}_2\text{O}_4$, as displayed in Fig. 3 A (inset). According to Mott-Schottky plots, E_{FB} (Fe_2O_3) and E_{FB} ($\text{Ov-NiFe}_2\text{O}_4$) could be obtained to be 0.15 eV and 0.24 eV (Fig. 3B, C), respectively, so the E_{CB} of Fe_2O_3 was 0.05 eV (vs. NHE) and the E_{VB} of $\text{Ov-NiFe}_2\text{O}_4$ was 0.34 eV (vs. NHE). Thus, the E_{VB} (Fe_2O_3) and E_{CB} ($\text{Ov-NiFe}_2\text{O}_4$) were respectively calculated to be 1.95 eV and –1.16 eV on the basis of the formula of $E_{CB} = E_{VB} - E_g$ [48]. The photoelectric properties of catalysts were studied. As shown in Fig. 3D-F, $\text{PDS-Fe}_2\text{O}_3 @\text{Ov-NiFe}_2\text{O}_4-\text{HR}$ shows the highest photocurrent response, the smallest circular radius and the lowest emission intensity better compared to the pure Fe_2O_3 and $\text{Ov-NiFe}_2\text{O}_4$. Because the unique hollow double shell structure could improve visible light absorption. In addition, O vacancies as the electrons trap could increase the concentration of charge carriers and accelerate photocarriers separation, and the Fe-O-Ni interface could facilitate the charge transfer between Fe_2O_3 and NiFe_2O_4 to improve the separation efficiency of charge carriers.

3.2. Photoelectrocatalytic synthesis of high value-added products H_2O_2

3.2.1. In situ generation of H_2O_2 on $\text{PDS-Fe}_2\text{O}_3 @\text{Ov-NiFe}_2\text{O}_4-\text{HR-Ti}$ photocathode

In order to study ORR process of the photocathode, the CV curves were applied to compare the ORR properties of Fe_2O_3 , $\text{Ov-NiFe}_2\text{O}_4$, $\text{PDS-Fe}_2\text{O}_3 @\text{Ov-NiFe}_2\text{O}_4-\text{HR}$ and $\text{PDS-Fe}_2\text{O}_3 @\text{Ov-NiFe}_2\text{O}_4-\text{HR-Ti}$ with light illumination (Fig. 4A). The $\text{PDS-Fe}_2\text{O}_3 @\text{Ov-NiFe}_2\text{O}_4-\text{HR}$ presented a more reactive ORR process compared to Fe_2O_3 or $\text{Ov-NiFe}_2\text{O}_4$ due to the formation of heterojunction, the unique hollow double shell structure, O vacancies and Fe-O-Ni interface could improve photocatalytic and electrolytic activity. Furthermore, the area of CV curves of the PDS-

$\text{Fe}_2\text{O}_3 @\text{Ov-NiFe}_2\text{O}_4-\text{HR-Ti}$ is larger than that of $\text{PDS-Fe}_2\text{O}_3 @\text{Ov-NiFe}_2\text{O}_4-\text{HR}$, indicating that the integrative $\text{PDS-Fe}_2\text{O}_3 @\text{Ov-NiFe}_2\text{O}_4-\text{HR-Ti}$ photocathode has excellent electrocatalytic activity and durability because strong binder-free binding with the Ti mesh could ensure the non-occurrence of wear or tear of the catalysts. The PEC activities of all the as-synthesized catalysts for H_2O_2 production were carried out in O_2 -saturated solution (pH = 3) with visible light irradiation. The PEC H_2O_2 production rates of $\text{PDS-Fe}_2\text{O}_3 @\text{Ov-NiFe}_2\text{O}_4-\text{HR-Ti}$ performance is up to 6.3 mM h⁻¹ (Fig. 4B), indicating that the large specific surface area, porous structure, hollow double-shell structure, O vacancies, the formation of interfaces of heterojunction and the integrative photocathode synergistically enhance PEC H_2O_2 production. It was also found that oxygen vacancies in the catalysts played a key role, catalysts with oxygen vacancy showed more efficient performance in PEC H_2O_2 production, indicating that oxygen vacancies could improve the separation efficiency of charge carriers to enhance PEC H_2O_2 generation.

The optimum PEC H_2O_2 production conditions of $\text{PDS-Fe}_2\text{O}_3 @\text{Ov-NiFe}_2\text{O}_4-\text{HR-Ti}$ for H_2O_2 production was achieved by varying the experimental conditions, such as electrolyte, potential and pH (Fig. S5), the yield of H_2O_2 could be obtained 21.5 mM for 3 h. To evaluate the stability and the ability of PEC catalysis with the $\text{PDS-Fe}_2\text{O}_3 @\text{Ov-NiFe}_2\text{O}_4-\text{HR-Ti}$ for producing H_2O_2 over 24 h was investigated. As shown in the Fig. 4C-D, the H_2O_2 cumulative amount is 152 mM, and the current is stable over 24 h. The XRD (Fig. S6) characterization manifests that the crystalline structure of the $\text{PDS-Fe}_2\text{O}_3 @\text{Ov-NiFe}_2\text{O}_4-\text{HR-Ti}$ keeps almost the same as the fresh one over 24 h. We compared the H_2O_2 production of the system with those of other reported materials in the literature (Fig. 4E), obviously, results suggest that the PEC H_2O_2 production of the $\text{PDS-Fe}_2\text{O}_3 @\text{Ov-NiFe}_2\text{O}_4-\text{HR-Ti}$ is much better than any other reported photoelectrocatalyst.

The above experimental results show that the $\text{PDS-Fe}_2\text{O}_3 @\text{Ov-NiFe}_2\text{O}_4-\text{HR-Ti}$ photocathode possesses excellent PEC ORR activity, durability and stability, so it has a good development prospect in practical production.

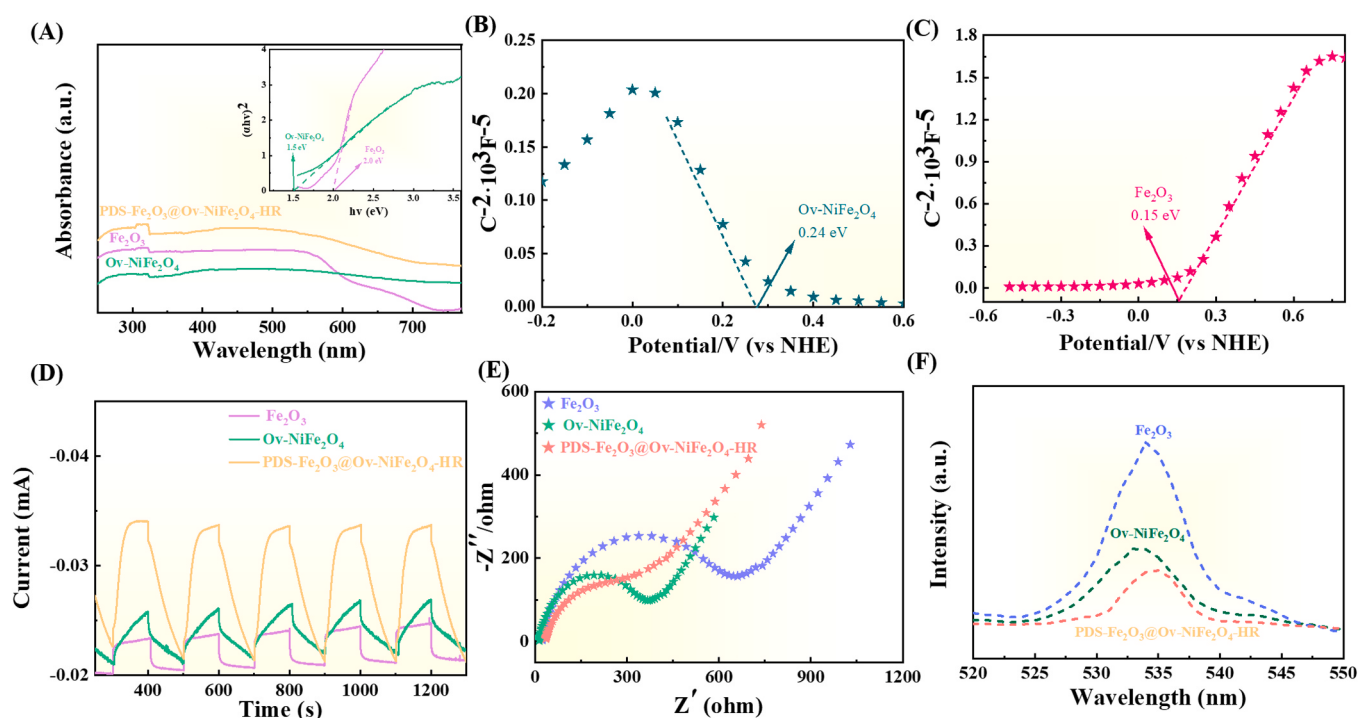


Fig. 3. (A) UV-vis DRS spectra of Fe_2O_3 , $\text{Ov-NiFe}_2\text{O}_4$ and $\text{PDS-Fe}_2\text{O}_3 @\text{Ov-NiFe}_2\text{O}_4-\text{HR}$, inset is the Kubelka-Munk plots converted from the UV-vis DRS spectra, the Mott-Schottky plots of (B) $\text{Ov-NiFe}_2\text{O}_4$ and (C) Fe_2O_3 , (D) Photocurrent response under visible light ($\lambda > 420 \text{ nm}$), (E) EIS Nyquist plots, (F) PL spectra of Fe_2O_3 , $\text{Ov-NiFe}_2\text{O}_4$ and $\text{PDS-Fe}_2\text{O}_3 @\text{Ov-NiFe}_2\text{O}_4-\text{HR}$.

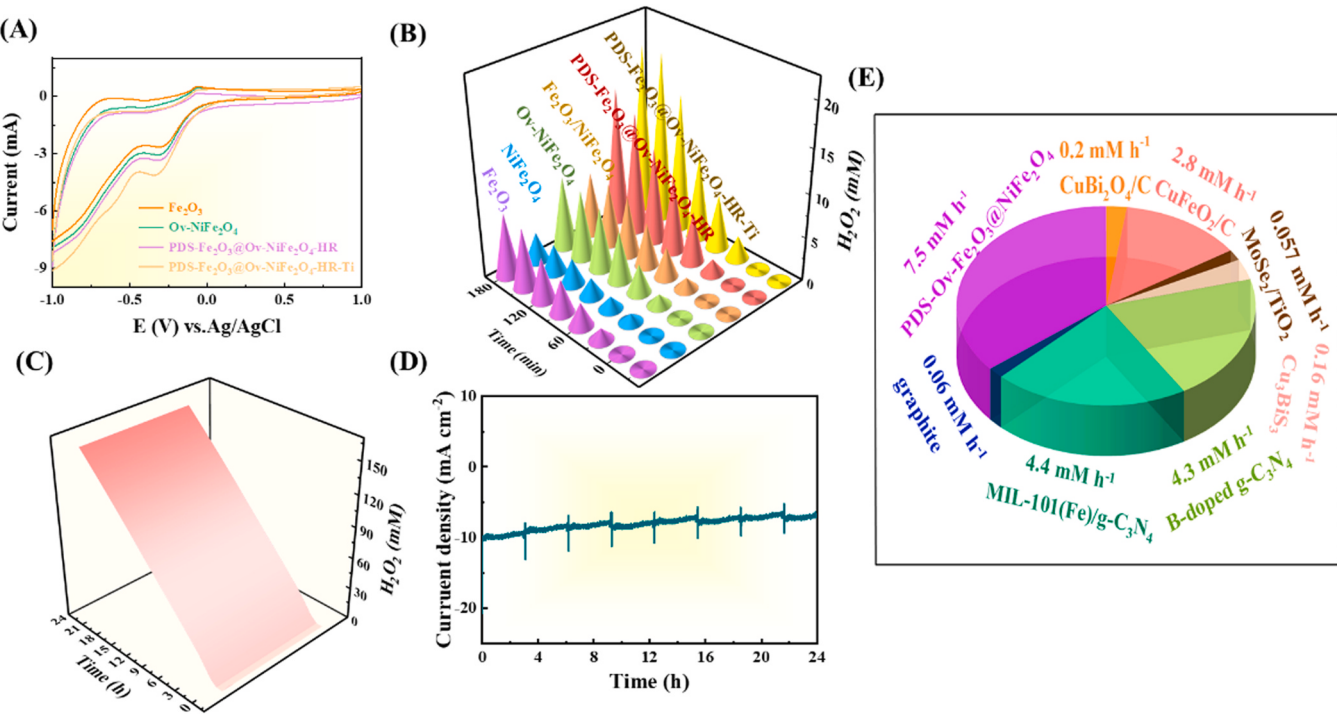


Fig. 4. Photoelectrocatalytic H₂O₂ production with different catalysts. (A) CV curves of Fe₂O₃, Ov-NiFe₂O₄, PDS-Fe₂O₃ @Ov-NiFe₂O₄-HR and PDS-Fe₂O₃ @Ov-NiFe₂O₄-HR-Ti under O₂ conditions, (B) Time-dependent H₂O₂ production, (C) Time-dependent H₂O₂ productions with PDS-Fe₂O₃ @Ov-NiFe₂O₄-HR-Ti (D) Time courses of the photocurrents, (E) Comparison with other catalysts for H₂O₂ production.

3.2.2. In situ generation of H₂O₂ on Fe₂O₃-Ti photoanode

Water oxidation ($2\text{H}_2\text{O} + 2\text{h}^+ \rightarrow \text{H}_2\text{O}_2 + 2\text{H}^+$, 1.77 V vs NHE) is H₂O₂ production of another cost-effective pathway. Based on this, the LSV of graphite carbon, Pt, WO₃, Sn₃O₄ and Fe₂O₃-Ti as photoanodes were investigated (Fig. 5 A), it was found that the Fe₂O₃-Ti had lower the onset potential and higher current density compared to other catalysts. So the Fe₂O₃-Ti was used as an anode for H₂O₂ production with WOR process. Simultaneously, the optimizing of electrolyte and potential can also increase H₂O₂ production (Fig. 5B-C). The higher H₂O₂ generation and higher faraday efficiency can be obtained in 0.1 M KHCO₃ as electrolyte (1.6 V_{NHE}).

3.2.3. Fe₂O₃-Ti // PDS-Fe₂O₃@Ov-NiFe₂O₄-HR-Ti simultaneous production of H₂O₂

An external bias (-0.5 V) was used between the two electrodes (photocathode PDS-Fe₂O₃ @Ov-NiFe₂O₄-HR-Ti, photoanode Fe₂O₃-Ti) under 1 sun illumination (Fig. 6 A). The yield of H₂O₂ on both electrodes

is shown in Fig. 6B, the concentration of H₂O₂ reached 12 mM at the cathode and 220 μM at the anode after 3 h of test. Furthermore, the Faradaic efficiency (FE) of H₂O₂ was estimated to be 80 %, which is greater in the half-cell electrolysis reactions (Fig. S7A). Obviously, Fe₂O₃-Ti and PDS-Ov-Fe₂O₃ @NiFe₂O₄-HR-Ti can be applied as highly efficient paired electrodes for simultaneous H₂O₂ production.

The LSV curves of the Fe₂O₃-Ti anode photoanode and PDS-Fe₂O₃ @Ov-NiFe₂O₄-HR-Ti photocathode were performed, because experimental parameters under the bias-free conditions could be predicted by comparing the LSVs of the photocathode and photoanode [49]. Fig. 6 C illustrates that the LSV curves of the photocathode and the photoanode intersect at 0.76 V_{NHE}. These results confirm above discussion that the system can be used to generate H₂O₂ without additional bias. Moreover, the PDS-Fe₂O₃ @Ov-NiFe₂O₄-HR-Ti also exhibits the highest photocurrents and photocurrents of 11 mA cm⁻² under the bias-free conditions (at E_{cell} = 0.0 V), as shown in Fig. 6D. Under this condition, the total H₂O₂ generation rate is 9.8 μmol min⁻¹ cm⁻², which is higher than any other

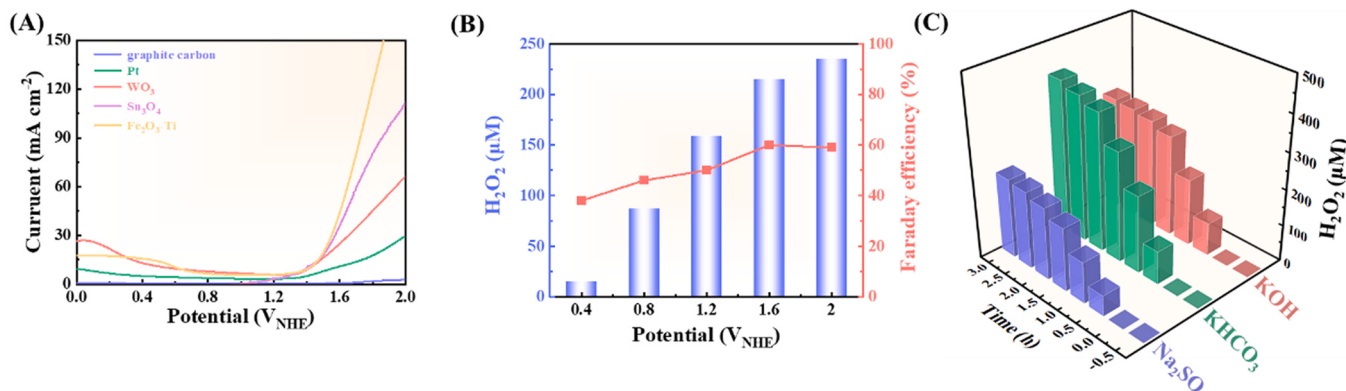


Fig. 5. (A) LSV curves with different electrodes, (B) Influence of different potential for H₂O₂ production, (C) Time-dependent H₂O₂ productions with different electrolytes.

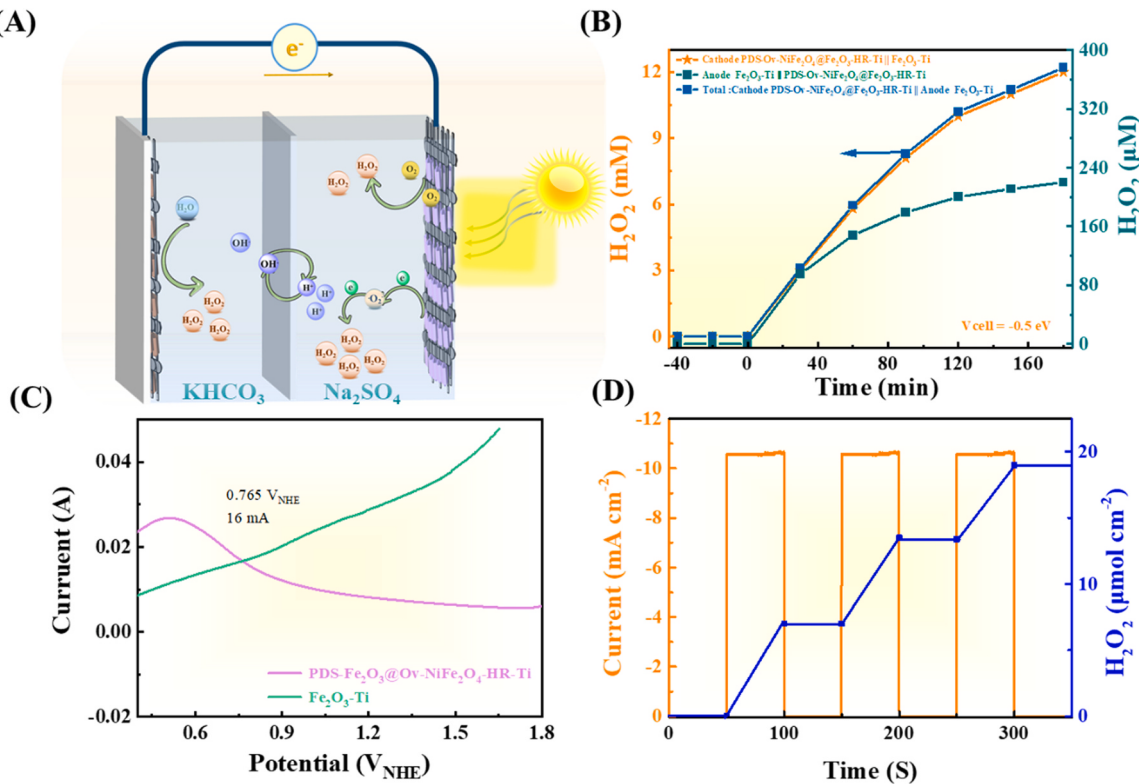


Fig. 6. (A) Schematic illustration of the design of light-driven cell with spontaneous H₂O₂ generation, (B) Time-dependent H₂O₂ productions by Fe₂O₃-Ti || PDS-Fe₂O₃ @Ov-NiFe₂O₄-HR-Ti, (C) The LSV curve of Fe₂O₃-Ti intersects with the reversed LSV curve of PDS-Fe₂O₃ @Ov-NiFe₂O₄-HR-Ti-cathode at 0.765 V_{NHE} under illumination, (D) The photocurrent-time profiles at E_{cell} = 0.0 V and H₂O₂ is spontaneously generated only under illumination.

recent reported PEC system for H₂O₂ production without external bias (Table 1). Furthermore, the current density of Fe₂O₃-Ti || PDS-Fe₂O₃ @Ov-NiFe₂O₄-HR-Ti has no obvious decay for 8 h (Fig. S7B), indicating it has long-term stability performance. Therefore, an eco-friendly method of the Light-Driven simultaneous H₂O₂ production only using sunlight, O₂ and water could be realized.

3.2.4. Mechanism of photoelectrocatalysis

To explore the reaction mechanism, free radical capture experiments were conducted to investigate active groups involved during the light-driven ORR process. It was found in Fig. 7 A that the H₂O₂ yield decreased with adding an electron scavenger (K₂S₂O₈), indicating that e⁻ was crucial active group for the production of H₂O₂. Similarly, the production of H₂O₂ also obviously declined in the presence of •O₂⁻ trapping agent (PBQ), confirming that •O₂⁻ was also the active group involved in the PEC process as well as the existence of a two-step single-electron ORR pathway to produce H₂O₂ (O₂ + e⁻ → •O₂⁻, -0.33 V_{NHE} and •O₂⁻ + 2 H⁺ + e⁻ → H₂O₂, 1.44 V_{NHE}). However, the H₂O₂ yield did not decrease with adding holes scavenger (oxalic acid), manifesting that holes did not play a role in PEC H₂O₂ production. To further explore pathways for PEC H₂O₂ production, the LSV of PDS-Fe₂O₃ @Ov-NiFe₂O₄-HR-Ti in an O₂-saturated solution at different rotating speeds by rotating ring disk electrode was recorded (RRDE, Fig. 7B). The data

obtained from Koutecky-Levich plots at a constant voltage (-0.9 V vs SCE) (Fig. 7 C) reveal that the number of electron transfer (n) in ORR is 1.72, which indicating that a two-electron ORR could exist PEC H₂O₂ production. Therefore, PDS-Fe₂O₃ @Ov-NiFe₂O₄-HR-Ti can produce H₂O₂ by a one-step two-electron (O₂ + 2 H⁺ + 2 e⁻ → H₂O₂, 0.695 V_{NHE}) and a two-step one electron ORR pathway (O₂ + e⁻ → •O₂⁻, -0.33 V_{NHE} and •O₂⁻ + 2 H⁺ + e⁻ → H₂O₂, 1.44 V_{NHE}).

According to the analysis of the above experimental results, if Fe₂O₃ and Ov-NiFe₂O₄ form a conventional type-II heterojunction, the photogenic e⁻ in the E_{CB} of Ov-NiFe₂O₄ would pass to the E_{CB} of Fe₂O₃, while h⁺ in the E_{VB} of Fe₂O₃ to the E_{VB} of Ov-NiFe₂O₄. However, the E_{CB} of Fe₂O₃ (0.05 V_{NHE}) was incapable of generating •O₂⁻ (-0.33 V_{NHE}), which was contradicted by the result of the •O₂⁻ capture experiment. Therefore, the photogenerated electrons of Fe₂O₃ combine with the photogenerated holes on Ov-NiFe₂O₄, which is in line with the Z-type charge transfer mechanism. Moreover, the open-circuit photovoltage (OCP) of the PEC test as a function of the separation efficiency of photogenerated charges was carried out. As shown in Fig. S8, PDS-Fe₂O₃ @Ov-NiFe₂O₄-HR-Ti has higher OCP values (Δ OCP = OCP_{dark} - OCP_{light}) in comparison with Fe₂O₃ and Ov-NiFe₂O₄ [52], indicating that Z-scheme heterojunction could form. Furthermore, based on the results of the above XPS analysis (Fig. 2), the binding energy of Fe 2p_{3/2} displays positive (0.6 eV) shift compared to Fe₂O₃, the bending energy of Ni

Table 1
Summary of H₂O₂ production in recent published photoelectrochemical systems.

Electrodes	Bias	H ₂ O ₂ production	H ₂ O ₂ generation type and electrode geometric area	Ref
BiVO ₄ C	no	3.2 μmol min ⁻¹ cm ⁻²	Two side generation from anode/cathode, 2 cm ⁻²	[6]
Fe(OOH)/BiVO ₄ CoII(Ch)	no	2.5 μmol min ⁻¹ cm ⁻²	One side generation from cathode 2.5 cm ⁻²	[12]
WO ₃ CoII(Ch)	no	1.6 μmol min ⁻¹ cm ⁻²	One side generation from cathode, 2.5 cm ⁻²	[50]
CoPi/BiVO ₄ Co-N/CNT	no	1.7 μmol min ⁻¹ cm ⁻²	One side generation from cathode, 3.4 cm ⁻²	[51]
Fe ₂ O ₃ Fe ₂ O ₃ @NiFe ₂ O ₄	no	9.8 μmol min ⁻¹ cm ⁻²	Two side generation from anode/cathode, 4 cm ⁻²	This work

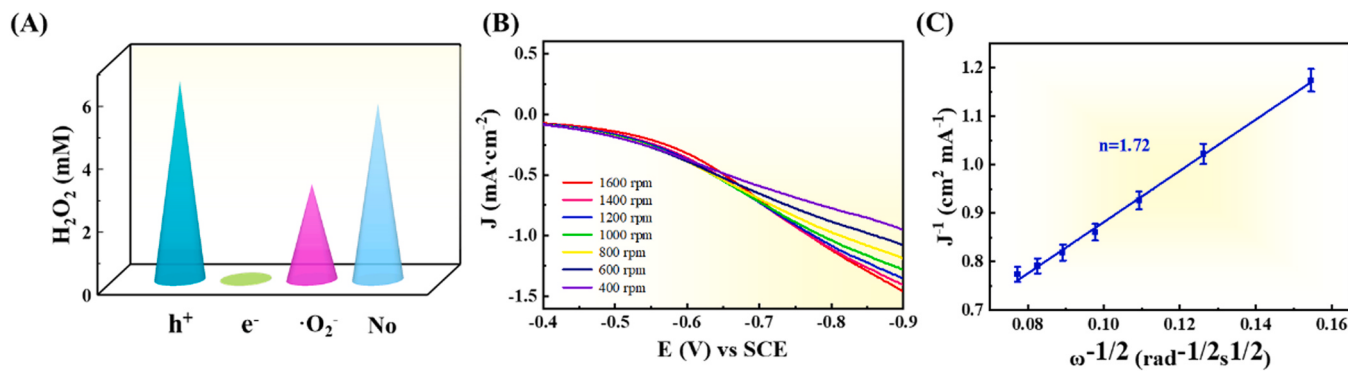


Fig. 7. (A) The influence of different scavengers on the PEC H_2O_2 production, (B) LSVs at different scan rates measured on RRDE, (C) The Koutecky-Levich plots of the data obtained by RRDE measurements in a buffered pH 3 solution with O_2 at -0.9 V_{SCE}.

$2\text{p}_{3/2}$ displays negative shift (0.2 eV) compared to Ov-NiFe₂O₄ and NiFe₂O₄, indicating that electrons were moved from Fe₂O₃ to NiFe₂O₄, also manifesting that the Z-scheme charge transfer exists on the PDS-Fe₂O₃ @Ov-NiFe₂O₄-HR-Ti photocathode. The introduction of Ov-NiFe₂O₄ catalysts is also beneficial to the enrichment of photo-generated electrons on O vacancies, which could promote the Z-type charge transfer mechanism to enhance the separation of photogenerated electron-hole pairs.

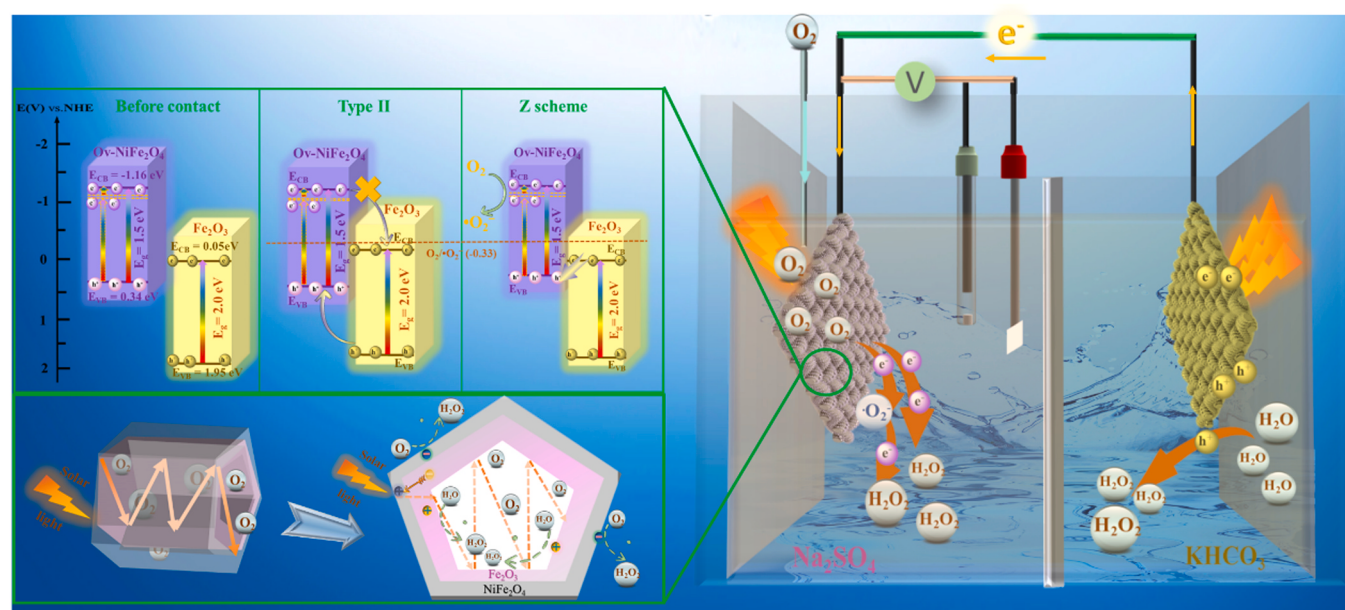
Simultaneously, Fe₂O₃-Ti can be excited along with photoelectrons and holes generation on the CB (-0.05 eV) and VB (1.95 eV) upon illumination. The holes of VB were applied for water oxidation ($2\text{H}_2\text{O} + 2\text{h}^+ \rightarrow \text{H}_2\text{O}_2 + 2\text{H}^+$, 1.77 V_{NHE}) producing H_2O_2 .

In conclusion, the integrated PDS-Fe₂O₃ @Ov-NiFe₂O₄-HR-Ti photocathode with excellent photoabsorption, faster charge transfer and excellent electrochemical activity was applied for PEC H_2O_2 production via ORR. Light-Driven Fe₂O₃-Ti || PDS-Fe₂O₃ @Ov-NiFe₂O₄-Ti simultaneous H_2O_2 production was shown in Scheme 2.

3.3. Photo-enhanced performance for rechargeable zinc- H_2O_2 batteries

Zn- H_2O_2 batteries could be constructed with PDS-Fe₂O₃ @Ov-NiFe₂O₄-HR-Ti photocathode for H_2O_2 production with alkaline (1 M KOH and 0.2 M ZnAc₂) (Fig. 8 A), the optimized Zn- H_2O_2 battery

exhibits superior high-rate discharging performance among 8.5 mW cm $^{-2}$ (Fig. 8B) and a high open-circuit voltage of 1.3 V (Fig. 8 C). As an application, two-serial Zn- H_2O_2 batteries can provide sufficient power to light a red LED. As shown in Fig. 8D, the processes I and II represent the first charging of a Zn- H_2O_2 battery with a platform, which is mainly accomplished by decomposition of H_2O_2 , oxidation of Fe^{2+} and Ni^{2+} . The process III and IV are the discharging process of Zn- H_2O_2 battery, which are mainly accomplished by ORR to H_2O_2 , reduction of Fe^{3+} and Ni^{3+} [33]. This battery has a relatively small charge-discharge voltage gap of 0.9 V at 10 mA cm $^{-2}$, attributing to the $\text{Ni}^{2+}/\text{Ni}^{3+}$ and $\text{Fe}^{2+}/\text{Fe}^{3+}$ redox pairs of the PDS-Fe₂O₃ @Ov-NiFe₂O₄-HR-Ti photocathode that could reduce the processes I plateau voltage and increases the process III plateau voltage, thereby improving battery energy efficiency [33]. To further validate the above experimental results, XPS spectra analysis of PDS-Fe₂O₃ @Ov-NiFe₂O₄-HR-Ti photocathode before and after test was performed (Fig. 8E), it was found that the Ni^{2+} and Fe^{2+} contents of PDS-Fe₂O₃ @Ov-NiFe₂O₄-HR-Ti after reaction changed compared to fresh PDS-Fe₂O₃ @Ov-NiFe₂O₄-HR-Ti. So $\text{Ni}^{2+}/\text{Ni}^{3+}$ and $\text{Fe}^{2+}/\text{Fe}^{3+}$ redox reactions are presented in the Zn- H_2O_2 battery, which is consistent with charge/discharge curves. To evaluate the stability of the assembled Zn- H_2O_2 batteries, the cyclic charge/discharge curves at a current density of 10 mA cm $^{-2}$ were tested (20 min for each cycle) (Fig. S9). Obviously, the PDS-Fe₂O₃ @Ov-NiFe₂O₄-HR-Ti



Scheme 2. Proposed reaction mechanism for H_2O_2 generation, and illustration of the design of light-driven fuel cell with spontaneous H_2O_2 generation.

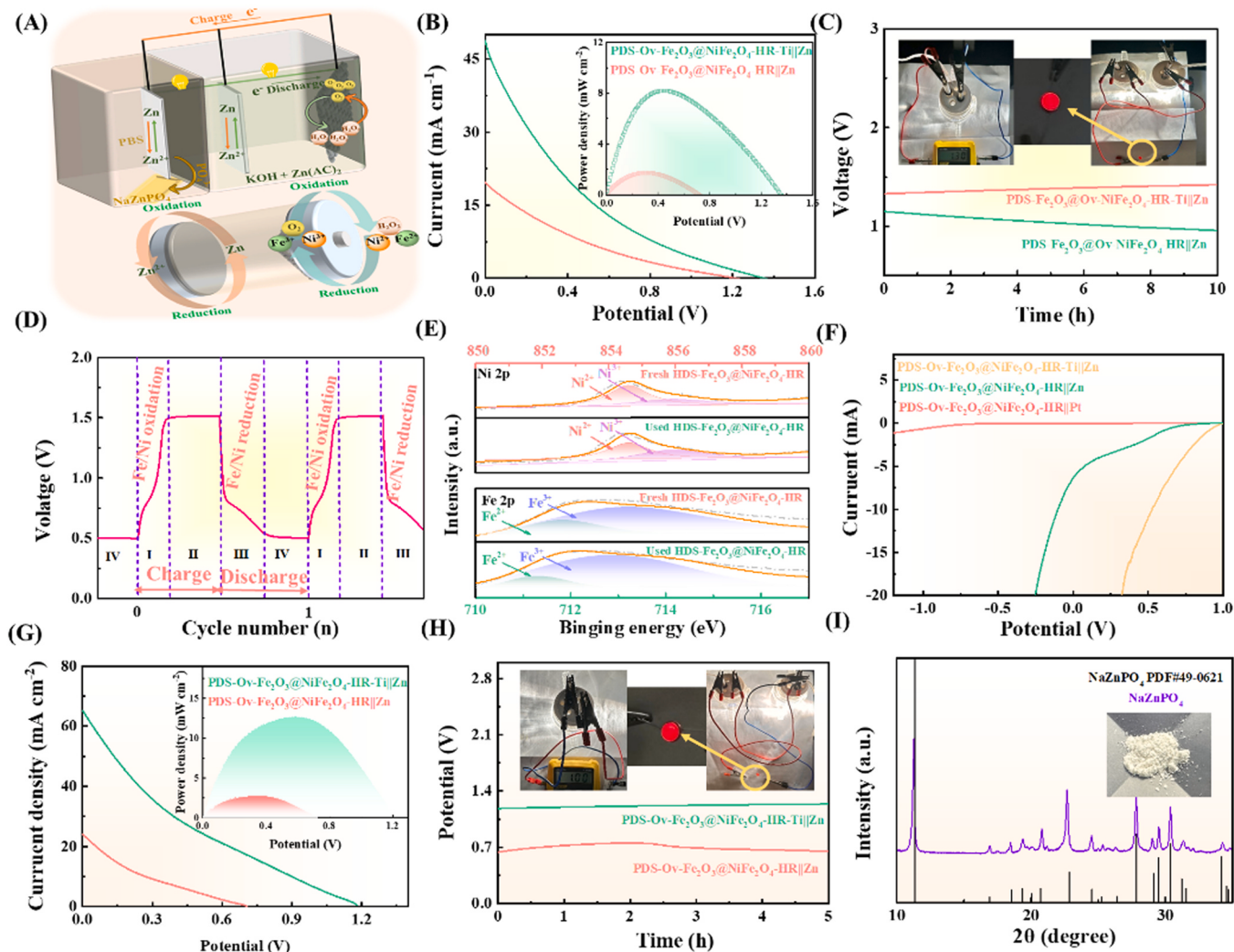


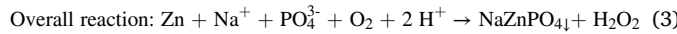
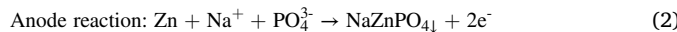
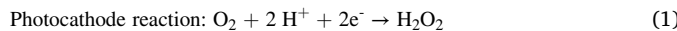
Fig. 8. (A) Schematic configuration of a single Zn-H₂O₂ battery with KOH+Zn(AC)₂ or PBS, (B) I-V curves of PDS-Fe₂O₃ @Ov-NiFe₂O₄-HR-Ti || Zn and PDS-Fe₂O₃ @Ov-NiFe₂O₄-HR || Zn with KOH+Zn(AC)₂ as electrolyte, inset is power density curves, (C) OCV curves of PDS-Fe₂O₃ @Ov-NiFe₂O₄-HR-Ti || Zn and PDS-Fe₂O₃ @Ov-NiFe₂O₄-HR || Zn with KOH+Zn(AC)₂ as electrolyte, inset is a series of two batteries power a LED, (D) The charge and discharge voltage curves of PDS-Fe₂O₃ @Ov-NiFe₂O₄-HR-Ti || Zn and PDS-Fe₂O₃ @Ov-NiFe₂O₄-HR || Zn, (E) XPS spectra of fresh and used PDS-Fe₂O₃ @Ov-NiFe₂O₄-HR: Fe 2p and Ni 2p, (F) The LSV of PDS-Fe₂O₃ @Ov-NiFe₂O₄-HR-Ti || Zn, PDS-Fe₂O₃ @Ov-NiFe₂O₄-HR || Zn and PDS-Fe₂O₃ @Ov-NiFe₂O₄-HR-Ti || Pt with PBS as electrolyte, (G) The I-V curves of PDS-Fe₂O₃ @Ov-NiFe₂O₄-HR-Ti || Zn and PDS-Fe₂O₃ @Ov-NiFe₂O₄-HR || Zn with PBS as electrolyte, inset is power density curves, (H) OCV curves of PDS-Fe₂O₃ @Ov-NiFe₂O₄-HR-Ti || Zn and PDS-Fe₂O₃ @Ov-NiFe₂O₄-HR || Zn with PBS as electrolyte, inset is a series of two batteries power a LED, (I) XRD pattern and photograph (inset) of NaZnPO₄.

of Zn-H₂O₂ battery can be maintained for over 100 h of charge/discharge testing without any significant decline in activity, compared to PDS-Fe₂O₃ @Ov-NiFe₂O₄-HR which has prominent voltage changes after 50 h of testing, indicating that integrative photocathode has excellent durability.

The Zn-H₂O₂ battery with PBS electrolyte (PO₄³⁻) instead of 1 M KOH alkaline electrolyte could not only realize energy conversion and storage, but also prepare heat-reflective materials of high value NaZnPO₄ precipitation. The PDS-Fe₂O₃ @Ov-NiFe₂O₄-HR-Ti as photocathode of Zn-H₂O₂ batteries with PBS electrolyte was performed (Fig. 8 A, Eqs. 1–3). To further explore the kinetics of the electrode reaction in the Zn-H₂O₂ battery with PBS electrolyte system, LSV curves were obtained in a two-electrode system equipped with different electrodes (Fig. 8 F). The LSV curve of PDS-Fe₂O₃ @Ov-NiFe₂O₄-HR-Ti || Zn system exhibits a potential output of + 0.5 V at a current density of 10 mA cm⁻², which is higher than the PDS-Fe₂O₃ @Ov-NiFe₂O₄-HR || Zn and PDS-Fe₂O₃ @Ov-NiFe₂O₄-HR-Ti || Pt system because the integrated PDS-Fe₂O₃ @Ov-NiFe₂O₄-HR-Ti photocathode has better electrocatalytic activity and corrosion resistance due to excellent conductivity and durability.

Discharging tests were performed at various current densities (Fig. S10), the Zn-H₂O₂ battery with PDS-Fe₂O₃ @Ov-NiFe₂O₄-HR-Ti photocathode showed stable voltage plateaus of 1.42–0.81 V at the discharge current density of 0.1–1.5 mA cm⁻², the extremely high operational stability of the system is attributing to O vacancies and strong coupling heterojunction interfaces as electrons transfer path which could enhance electrons transfer efficiency. The OCV of the PDS-Fe₂O₃ @Ov-NiFe₂O₄-HR-Ti || Zn can be maintained at higher than 1.0 V for more than 5 h (Fig. 8 H). The resultant power density of the PDS-Fe₂O₃ @Ov-NiFe₂O₄-HR-Ti || Zn cell indicated that a peak power density of 12 mW cm⁻² at 0.47 V (Fig. 8 G), two PDS-Fe₂O₃ @Ov-NiFe₂O₄-HR-Ti || Zn systems connected in series can also provide sufficient power to light a LED (Fig. 8 H). The XRD pattern of products (NaZnPO₄) was shown in Fig. 8 I, the corresponding reflections are located at 11.37°, 16.91°, 20.62°, 22.85°, 29.15°, 31.84°, and 34.20° which belong to the (101), (110), (112), (202), (114), (302), and (220) planes NaZnPO₄ (PDF: 49-0621), respectively. In summary, the multifunctional PDS-Fe₂O₃ @Ov-NiFe₂O₄-HR-Ti photocathode constructed Zn- H₂O₂ battery not only produces H₂O₂ and high-value-added NaZnPO₄, but also has a considerable

electric power output, which provides considerable development prospects for the development of energy saving and environmental protection photoelectric catalysis.



4. Conclusion

In this study, an efficient photocathode of intriguing synthesis strategy and well-controlled structure conducted PDS-Fe₂O₃ @Ov-NiFe₂O₄-HR-Ti was fabricated with a high yield of H₂O₂ (152 mM, 24 h) and good Faraday efficiency (80%). Owing to porous double-shell hollow structure, abundant O vacancies, Z-scheme strong coupling heterojunction interfaces, there are enhanced consequently light absorption, separation efficiency and high redox capability of photo-excited carriers. The PDS-Fe₂O₃ @Ov-NiFe₂O₄-HR-Ti photocathode and the Fe₂O₃-Ti anode combined to fabricate PEC system enabled sustained H₂O₂ generation (13.2 Mm, 3 h) on both electrodes. The dual electrode system also successfully demonstrated H₂O₂ production under an external bias-free condition (9.8 μmol min⁻¹ cm⁻²). Simultaneously, the PDS-Fe₂O₃ @Ov-NiFe₂O₄-HR-Ti photocathode for rechargeable Zn-H₂O₂ batteries presents a high power density of 12 mW cm⁻² and high-value chemicals NaZnPO₄. Obviously, the present study provides a new strategy for constructing highly efficient heterostructure photocathode for the PEC process, which can be the guidance for another photocathode materials design and displays a viable strategy for multifunctional photoelectrocatalysts on energy-related devices.

CRediT authorship contribution statement

Xue Feng: Conceptualization, Methodology, Validation, Formal analysis, Investigation, Data curation, Writing – original draft, Writing – review & editing, Visualization. **Lei Zhang:** Conceptualization, Resources, Supervision, Project administration, Funding acquisition.

Declaration of Competing Interest

The authors declare that they have no known competing financial interests or personal relationships that could have appeared to influence the work reported in this paper.

Data availability

The authors are unable or have chosen not to specify which data has been used.

Acknowledgements

This project was supported by the National Nature Science Foundation of China (NSFC52072164 and 52102104), and Liaoning Revitalization Talents Program (No. XLYC1902066), China. The authors also thank their colleagues and other students who participated in this study.

Appendix A. Supporting information

Supplementary data associated with this article can be found in the online version at [doi:10.1016/j.apcatb.2023.122955](https://doi.org/10.1016/j.apcatb.2023.122955).

References

- [1] A.D. Bokare, W. Choi, Review of iron-free Fenton-like systems for activating H₂O₂ in advanced oxidation processes, *J. Hazard. Mater.* 275 (2014) 121–135, <https://doi.org/10.1016/j.jhazmat.2014.04.054>.
- [2] S. Fukuzumi, Y. Yamada, Hydrogen peroxide used as a solar fuel in one-compartment fuel cells, *ChemElectroChem* 3 (2016) 1978–1989, <https://doi.org/10.1002/celec.201600317>.
- [3] D. Kim, K.K. Sakimoto, D.C. Hong, P.D. Yang, Artificial photosynthesis for sustainable fuel and chemical production, *Angew. Chem. Int. Ed.* 54 (2015) 3259–3266, <https://doi.org/10.1002/anie.201409116>.
- [4] M. Antoniadou, P. Lianos, Production of electricity by photoelectrochemical oxidation of ethanol in a PhotoFuelCell, *Appl. Catal. B Environ.* 99 (2010) 307, <https://doi.org/10.1016/j.apcatb.2010.06.037>.
- [5] H. Wu, T. He, M. Dan, L. Du, N. Li, Z.Q. Liu, Activated Ni-based metal-organic framework catalyst with well-defined structure for electrosynthesis of hydrogen peroxide, *Chem. Eng. J.* 435 (2022), 134863, <https://doi.org/10.1016/j.cej.2022.134863>.
- [6] X. Shi, Y. Zhang, S. Siahrostami, X. Zheng, Light-driven BiVO₄-C fuel cell with simultaneous production of H₂O₂, *Adv. Energy Mater.* 23 (2018), 1801158, <https://doi.org/10.1002/aenm.201801158>.
- [7] X. Hu, X. Zeng, Y. Liu, J. Lu, X. Zhang, Carbon-based materials for photo- and electrocatalytic synthesis of hydrogen peroxide, *Nanoscale* 12 (2020) 16008, <https://doi.org/10.1039/DONR03178J>.
- [8] J. y Chen, L. Zhao, N. Li, H. Liu, A microbial fuel cell with the three-dimensional electrode applied an external voltage for synthesis of hydrogen peroxide from organic matter, *J. Power Sources* 287 (2015) 291, <https://doi.org/10.1016/j.jpowsour.2015.04.071>.
- [9] M. Dan, R. Zhong, S. Hu, H. Wu, Y. Zhou, Z. Liu, Strategies and challenges on selective electrochemical hydrogen peroxide production: catalyst and reaction medium design, *Chem. Catal.* 2 (2022) 1919–1960, <https://doi.org/10.1016/j.cheat.2022.06.002>.
- [10] C. Chen, M. Yasugi, L. Yu, Z. Teng, T. Ohno, Visible light-driven H₂O₂ synthesis by a Cu₃BiS₃ photocathode via a photoelectrochemical indirect two-electron oxygen reduction reaction, *Appl. Catal. B Environ.* 307 (2022), 121152, <https://doi.org/10.1016/j.apcatb.2022.121152>.
- [11] M. Sun, B. Liu, W. Han, Z. Zhang, M. Xie, CuBi₂O₄ photocathode with integrated electric field for enhanced H₂O₂ production, *Appl. Catal. B Environ.* 304 (2022), 120980, <https://doi.org/10.1016/j.apcatb.2021.120980>.
- [12] X. Zhang, Y. Zeng, W. Shi, Z. Tao, J. Liao, C. Ai, H. Si, Z. Wang, A.C. Fisher, S. Lin, S-scheme heterojunction of core–shell biphasic (¹T₁–²H)-MoSe₂/TiO₂ nanorod arrays for enhanced photoelectrocatalytic production of hydrogen peroxide, *Chem. Eng. J.* 429 (2022), 131312, <https://doi.org/10.1016/j.cej.2021.131312>.
- [13] J.G. Rostra, J.C. Seoane, Q. Guo, A.B.J. Sobrido, A.R.G. Elipe, A. Borras, Photoelectrochemical water splitting with ITO/WO₃/BiVO₄/CoPi multishell nanotubes enabled by a vacuum and plasma soft-template synthesis, *Appl. Mater. Interfaces* 15 (2023) 9250–9262, <https://doi.org/10.1021/acsami.2c19868>.
- [14] I. Abdellaoui, M.M. Islam, M. Remehka, S. Kanno, R. Okamoto, K. Tajima, S. A. Pawar, Y.H. Ng, C. Budich, T. Maeda, T. Wada, S. Ikeda, T. Sakurai, Mechanism of incorporation of zirconium into BiVO₄ visible-light photocatalyst, *J. Phys. Chem. C* 125 (2021) 3320–3326, <https://doi.org/10.1021/acs.jpcc.1c00339>.
- [15] C. Cheng, Q. Shi, W. Zhu, Y. Zhang, W. Su, Z. Lu, J. Yan, K. Chen, Q. Wang, J. Li, Microwave-assisted synthesis of MoS₂/BiVO₄ heterojunction for photocatalytic degradation of tetracycline hydrochloride, *Nanomaterials* 13 (2023) 1522, <https://doi.org/10.3390/nano13091522>.
- [16] K. Mase, M. Yoneda, Y. Yamada, S. Fukuzumi, Efficient photocatalytic production of hydrogen peroxide from water and dioxygen with bismuth vanadate and a cobalt(II) chlorin complex, *ACS Energy Lett.* 1 (2016) 913, <https://doi.org/10.1021/acsenergylett.6b00415>.
- [17] K. Fuku, Y. Miyase, Y. Miseki, T. Funaki, T. Gunji, K. Sayama, Photoelectrochemical hydrogen peroxide production from water on a WO₃/BiVO₄ photoanode and from O₂ on an Au cathode without external bias, *Chem. Asian J.* 12 (2017) 1111, <https://doi.org/10.1002/asia.201700292>.
- [18] M. Xiao, Z. Wang, M. Lyu, B. Luo, S. Wang, G. Liu, H. Cheng, L. Wang, Hollow nanostructures for photocatalysis: advantages and challenges, *Adv. Mater.* (2018), 1801369, <https://doi.org/10.1002/adma.201801369>.
- [19] X. Wang, J. Feng, Y. Bai, Q. Zhang, Y. Yin, Synthesis, properties, and applications of hollow micro-/nanostructures, *Chem. Rev.* 116 (2016) 10983, <https://doi.org/10.1021/acs.chemrev.5b00731>.
- [20] G. Prieto, H. Tuysuz, N. Duyckaerts, J. Knossalla, G.-H. Wang, F. Schüth, Hollow nano- and microstructures as catalysts, *Chem. Rev.* 116 (2016) 14056, <https://doi.org/10.1021/acs.chemrev.6b00374>.
- [21] N.Q. Tran, T.A. Le, H. Kim, Y. Hong, Y. Cho, G.H. Park, H. Kim, M. Kim, J. Lee, W. S. Yoon, H. Lee, Low iridium content confined inside a Co₃O₄ hollow sphere for superior acidic water oxidation, *ACS Sustain. Chem. Eng.* 19 (2019) 16640–16650, <https://doi.org/10.1021/acssuschemeng.9b03982>.
- [22] X. Feng, Q. Jiao, W. Chen, Y. Dang, Z. Dai, S.L. Suib, J. Zhang, Y. Zhao, H. Li, C. Feng, Cactus-like NiCo₂S₄@NiFe LDH hollow spheres as an effective oxygen bifunctional electrocatalyst in alkaline solution, *Appl. Catal. B Environ.* 286 (2021), 119869, <https://doi.org/10.1016/j.apcatb.2020.119869>.
- [23] R. Ma, L. Wang, H. Wang, Z. Liu, M. Xing, L. Zhu, X. Meng, F.S. Xiao, Solid acids accelerate the photocatalytic hydrogen peroxide synthesis over a hybrid catalyst of titania nanotube with carbon dot, *Appl. Catal. B Environ.* 244 (2019) 594–603, <https://doi.org/10.1016/j.apcatb.2018.11.087>.
- [24] L. Zhang, J. Liang, L. Yue, K. Dong, Z. Xu, T. Li, Q. Liu, Y. Luo, Y. Liu, S. Gao, A. M. Asiri, Q. Kong, X. Guo, X. Sun, CoTe nanoparticle-embedded N-doped hollow

- carbon polyhedron: an efficient catalyst for H_2O_2 electrosynthesis in acidic media, *J. Mater. Chem. A* 9 (2021) 21703–21707, <https://doi.org/10.1039/D1TA06313H>.
- [25] J. Di, B. Lin, B. Tang, S. Guo, J. Zhou, Z. Liu, Engineering cocatalysts onto low-dimensional photocatalysts for CO_2 reduction, *Small Struct.* 2 (2021), 2100046, <https://doi.org/10.1002/sstr.202100046>.
- [26] S. Li, L. Zhang, W. Zhao, S. Yuan, L. Yang, X. Chen, P. Ge, W. Sun, X. Ji, Designing interfacial chemical bonds towards advanced metal-based energy-storage/conversion materials, *Energy Stor. Mater.* 32 (2020) 477–496, <https://doi.org/10.1016/j.ensm.2020.07.023>.
- [27] Y. Zhang, J. Di, X. Zhu, M. Ji, C. Chen, Y. Liu, L. Li, T. Wei, H. Li, J. Xia, Chemical bonding interface in $\text{Bi}_2\text{Sn}_2\text{O}_7/\text{BiOBr}$ S-scheme heterojunction triggering efficient N_2 photofixation, *Appl. Catal. B Environ.* 323 (2023), 122148, <https://doi.org/10.1016/j.apcatb.2022.122148>.
- [28] X. Wang, X. Wang, J. Huang, Interfacial chemical bond and internal electric field modulated Z-scheme $\text{Sv-ZnIn}_2\text{S}_4/\text{MoSe}_2$ photocatalyst for efficient hydrogen evolution, *Nat. Commun.* 12 (2021) 4112, <https://doi.org/10.1038/s41467-021-24511-z>.
- [29] J. Li, F. Wei, Z. Xiu, X. Han, Direct Z-scheme charge transfer of $\text{Bi}_2\text{WO}_6/\text{InVO}_4$ interface for efficient photocatalytic CO_2 reduction, *Chem. Eng. J.* 446 (2022), 137129, <https://doi.org/10.1016/j.cej.2022.137129>.
- [30] S. Huang, T. Ouyang, B.F. Zheng, M. Dan, Z.Q. Liu, Enhanced photoelectrocatalytic activities for CH_3OH -to-HCHO conversion on $\text{Fe}_2\text{O}_3/\text{MoO}_3$: Fe-O-Mo covalency dominates the intrinsic activity, *Angew. Chem. Int. Ed.* 60 (2021) 9546–9552, <https://doi.org/10.1002/anie.202101058>.
- [31] Y.J. Wu, J. Yang, T.X. Tu, W.Q. Li, P.F. Zhang, Y. Zhou, J. Li, J.T. Li, S.G. Sun, Evolution of cationic vacancy defects: a motif for surface restructuration of OER precatalyst, *Angew. Chem. Int. Ed.* 60 (2021) 26829–26836, <https://doi.org/10.1002/anie.202112447>.
- [32] Z. Sun, L. Lin, J. He, D. Ding, T. Wang, J. Li, M. Li, Y. Liu, Y. Li, M. Yuan, B. Huang, H. Li, G. Sun, Regulating the spin state of Fe^{III} enhances the magnetic effect of the molecular catalysis mechanism, *J. Am. Chem. Soc.* 144 (2022) 8204–8213, <https://doi.org/10.1021/jacs.2c01153>.
- [33] J. Zhang, J. Lian, Q. Jiang, G. Wang, Boosting the OER/ORR/HER activity of Ru-doped Ni/Co oxides heterostructure, *Chem. Eng. J.* 439 (2022), 135634, <https://doi.org/10.1016/j.cej.2022.135634>.
- [34] G. Zhang, X. Liu, L. Wang, G. Xing, C. Tian, H. Fu, Copper collector generated $\text{Cu}^+/\text{Cu}^{2+}$ redox pair for enhanced efficiency and lifetime of Zn-Ni/air hybrid battery, *ACS Nano* 16 (2022) 17139–17148, <https://doi.org/10.1021/acsnano.2c07542>.
- [35] S. Du, Z. Ren, X. Wang, J. Wu, H. Meng, H. Fu, Controlled atmosphere corrosion engineering toward inhomogeneous NiFe-LDH for energetic oxygen evolution, *ACS Nano* 16 (2022) 7794–7803, <https://doi.org/10.1021/acsnano.2c00332>.
- [36] C. Li, M. Li, S. Yin, L. Zeng, L. Zhang, Electrochemical performance enhancement by the partial reduction of $\text{NiFe}_2\text{O}_4@\text{g-C}_3\text{N}_4$ with core-shell hollow structure, *J. Alloy. Compd.* 861 (2021), 157986, <https://doi.org/10.1016/j.jallcom.2020.157986>.
- [37] X. Yu, Z. Zhao, D. Sun, N. Ren, J. Yu, R. Yang, H. Liu, Microwave-assisted hydrothermal synthesis of Sn_3O_4 nanosheet/rGO planar heterostructure for efficient photocatalytic hydrogen generation, *Appl. Catal. B Environ.* 227 (2018) 470–476, <https://doi.org/10.1016/j.apcatb.2018.01.055>.
- [38] B. Lei, W. Cui, P. Chen, L. Chen, J. Li, F. Dong, C-doping induced oxygen-vacancy in WO_3 nanosheets for CO_2 activation and photoreduction, *ACS Catal.* 12 (2022) 9670–9678, <https://doi.org/10.1021/acscatal.2c02390>.
- [39] S. Huang, F. Feng, R.T. Huang, T. Ouyang, J. Liu, Z.Q. Liu, Activating C-H bonds by tuning Fe sites and an interfacial effect for enhanced methanol oxidation, *Adv. Mater.* 34 (2022), 2208438, <https://doi.org/10.1002/adma.202208438>.
- [40] Y. Wang, S. Wang, S.L. Zhang, X.W. Lou, Formation of hierarchical $\text{FeCoS}_2-\text{CoS}_2$ double-shelled nanotubes with enhanced performance for photocatalytic reduction of CO_2 , *Angew. Chem. Int. Ed.* 59 (2020) 11918–11922, <https://doi.org/10.1002/anie.202004609>.
- [41] L. Zhang, H.B. Wu, X.W. Lou, Metal-organic-frameworks-derived general formation of hollow structures with high complexity, *J. Am. Chem. Soc.* 135 (2013) 10664–10672, <https://doi.org/10.1021/ja401727n>.
- [42] Z. Gao, Y. Li, C. Zhang, S. Zhang, Y. Jia, Y. Dong, An enzyme-free immunosensor for sensitive determination of procalcitonin using NiFe PBA nanocubes@TB as the sensing matrix, *Anal. Chim. Acta* 1097 (2020) 169–175, <https://doi.org/10.1016/j.aca.2019.11.003>.
- [43] Y. Wang, X. Guo, Z. Wang, M. Liu, Bin Wu, Y. Wang, C. Yan, A. Yuan, H. Yang, Controlled pyrolysis of MIL-88A to $\text{Fe}_2\text{O}_3@\text{C}$ nanocomposites with varied morphologies and phases for advanced lithium storage, *J. Mater. Chem. A* 5 (2017) 25562–25573, <https://doi.org/10.1016/j.aca.2019.11.003>.
- [44] J. Liu, D. Zhu, T. Ling, A. Vasileff, S.Z. Qiao, S-Ni Fe_2O_4 ultra-small nanoparticle built nanosheets for efficient water splitting in alkaline and neutral pH, *Nano Energy* 40 (2017) 264–273, <https://doi.org/10.1016/j.nanoen.2017.08.031>.
- [45] W. Xu, W. Tian, L. Meng, F. Cao, L. Li, Interfacial chemical bond-modulated Z-scheme charge transfer for efficient photoelectrochemical water splitting, *Adv. Energy Mater.* 11 (2021), e20203500, <https://doi.org/10.1002/aenm.202003500>.
- [46] C. Li, L.J. Xie, J.W. Zhao, L.F. Gu, H.B. Tang, L. Zheng, G.R. Li, Interfacial Fe-O-Ni-O-Fe bonding regulates the active Ni sites of Ni-MOFs via iron doping and decorating with FeOOH for super efficient oxygen evolution, *Angew. Chem. Int. Ed.* 61 (2022), e202116934, <https://doi.org/10.1002/ange.202116934>.
- [47] X. Hu, J. Wang, J. Wang, Y. Deng, H. Zhang, T. Xu, W. Wang, β particles induced directional inward migration of oxygen vacancies: surface oxygen vacancies and interface oxygen vacancies synergistically activate PMS, *Appl. Catal. B Environ.* 318 (2022), 121879, <https://doi.org/10.1016/j.apcatb.2022.121879>.
- [48] X. Liu, D. Xu, D. Zhang, Superior performance of 3 D Co-Ni bimetallic oxides for catalytic degradation of organic dye: investigation on the effect of catalyst morphology and catalytic mechanism, *Appl. Catal. B Environ.* 186 (2016) 193–203, <https://doi.org/10.1016/j.apcatb.2016.01.005>.
- [49] T.H. Jeon, H. Kim, H. Kim, W. Choi, Highly durable photoelectrochemical H_2O_2 production via dual photoanode and cathode processes under solar simulating and external bias-free conditions, *Energy Environ. Sci.* 13 (2020) 1730–1742, <https://doi.org/10.1039/C9EE03154E>.
- [50] K. Mase, M. Yoneda, Y. Yamada, S. Fukuzumi, Seawater usable for production and consumption of hydrogen peroxide as a solar fuel, *Nat. Commun.* 7 (2016) 11470, <https://doi.org/10.1038/ncomms11470>.
- [51] M. Kol, Y. Kim1, J. Woo, B. Lee, R. Mehrotra, P. Sharma, J. Kim, S.W. Hwang, H. Y. Jeong, H. Lim, S.H. Joo, J.W. Jang, J.H. Kwak, Direct propylene epoxidation with oxygen using a photo-electro-heterogeneous catalytic system, *nat. Catal.* 5 (2022) 37–44, <https://doi.org/10.6084/m9.figshare.16936906>.
- [52] Y. Li, Q. Wu, Y. Chen, R. Zhang, C. L, K. Zhang, M. Li, Y. Lin, D. Wang, X. Zou, T. Xie, Interface engineering Z-scheme $\text{Ti}-\text{Fe}_2\text{O}_3/\text{In}_2\text{O}_3$ photoanode for highly efficient photoelectrochemical water splitting, *Appl. Catal. B Environ.* 290 (2021), 120058, <https://doi.org/10.1016/j.apcatb.2021.120058>.